9. Blase, X., Adessi, Ch. & Connetable, D. Role of the dopant in the superconductivity of diamond. Phys. Rev. Lett. 93, 237004 (2004).
10. Nebel, C. E. & Ristein, J. Thin-film Diamond II Ch. 4–8, 121–358 (Elsevier, Amsterdam, 2004).
11. Zunger, A. & Freeman, A. J. Ground-state electronic properties of diamond in the local-density formalism. Phys. Rev. B 15, 5049–5065 (1977).
12. Collins, A. T. & Williams, A. W. S. The nature of the acceptor centre in semiconducting diamond. J. Phys. C 4, 1789–1800 (1971).
13. Kamakura, N. et al. Layer dependent band dispersion and correlation using soft X-ray ARPES. Europhys. Lett. 67, 240–246 (2004).
14. Inglesfield, J. E. & Plummer, E. W. in Angle-resolved Photoemission (ed. Kevan, S. D.) Ch. 2, 15–61 (Elsevier, Amsterdam, 1992).
15. Gravell, R. G. et al. X-ray photoemission cross-section modulation in Diamond, Silicon, Germanium, Methane, Silane, and Germane. Phys. Rev. B 7, 5313–5316 (1973).
16. Matsushita, T. et al. Angle-resolved soft X-ray photoemission for the valence band of graphite. Surf. Rev. Lett. 9, 1321–1326 (2002).
17. Jimenez, I. et al. Accurate valence band width of diamond. Phys. Rev. B 56, 7215–7221 (1997).
18. Nakamura, J. et al. Holes in the valence band of superconducting boron-doped diamond film studied by soft X-ray absorption and emission spectroscopy. Preprint at ⟨http://arXiv.org/cond-mat/0410144⟩ (2004).
19. Campuzano, J. C., Norman, M. R. & Randeria, M. The Physics of Superconductors Vol. II, Ch. 5, 184 (Springer, Berlin/Heidelberg, 2004).
20. Umezawa, H. et al. Advantage on superconductivity of heavily boron-doped (111) diamond films. Preprint at ⟨http://arXiv.org/cond-mat/0503303⟩ (2004).

LETTERS

Chemically tailorable colloidal particles from infinite coordination polymers

Moonhyun Oh[1] & Chad A. Mirkin[1]

Micrometre- and nanometre-sized particles play important roles in many applications, including catalysis[1], optics[2,3], biosensing[4–8] and data storage[9]. Organic particles[10] are usually prepared through polymerization of suitable monomers[11] or precipitation methods[12]. In the case of inorganic materials, particle fabrication tends to involve the reduction of a metal salt[13], or the controlled mixing of salt solutions supplying a metal cation and an elemental anion (for example, S^{2-}, Se^{2-}, O^{2-})[14], respectively; in some instances, these methods even afford direct control over the shape of the particles produced[16,17]. Another class of materials are metal-organic coordination polymers[18–23], which are based on metal ions coordinated by polydentate organic ligands and explored for potential use in catalysis[18], gas storage[19,20], nonlinear optics[21] and molecular recognition and separations[22,23]. In a subset of these materials, the use of organometallic complexes as ligands (so-called metalloligands) provides an additional level of tailorability, but these materials have so far not yet been fashioned into nano- or microparticles. Here we show that simple addition of an initiation solvent to a precursor solution of metal ions and metalloligands results in the spontaneous and fully reversible formation of a new class of metal–metalloligand particles. We observe initial formation of particles with diameters of a few hundred nanometres, which then coalesce and anneal into uniform and smooth microparticles. The ease with which these particles can be fabricated, and the ability to tailor their chemical and physical properties through the choice of metal and organic ligand used, should facilitate investigations of their scope for practical applications.

We have discovered that spherical micro- and nanoparticles composed of polymerized metal-ligand networks can be made by the coordination-chemistry-induced assembly of metal ions and homochiral carboxylate-functionalized binapthyl bis-metallo-tridentate Schiff base (BMSB) building blocks (Fig. 1). In a typical experiment, a precursor pyridine solution consisting of a 1:1 mixture of the appropriate metal acetate salt ($M'(OAc)_2$, $M' = Zn$, Cu and Ni, 1) and BMSB, 2, is prepared (alternatively, a 3:1 mixture of 1 and enantiopure carboxylate-functionalized binapthyl bis-tridentate Schiff base (BSB) can be used). Slow addition of an initiation solvent such as diethyl ether or pentane results in the spontaneous formation of spherical inorganic polymer particles, 3. These particles form via coordination of the carboxylate groups on the BMSB precursor with the metal ions supplied by the acetate salt, and the polymerization process is completely reversible, as evidenced by the formation of the starting materials upon addition of excess pyridine (Fig. 1).

The homochiral BMSB building blocks 2a–c are key components which are readily polymerizable through their carboxylate groups; the choice of BMSB ligand, type of metallation, and ancillary ligands makes it possible to manipulate the chemical and physical properties of the resulting structures 3 in a systematic manner. The BMSB building blocks were prepared from the reaction of two equivalents of $M(OAc)_2$ ($M = Zn$, Cu and Ni) and one equivalent of BSB in a N,N-dimethylformamide (DMF) solution at room temperature. The building blocks 2a–c have been characterized by ^{1}H NMR, ^{13}C NMR, infrared spectroscopy and electrospray ionization mass spectrometry, and all data are consistent with the proposed structures. Compound 2b also was characterized in the solid state by a single-crystal X-ray diffraction study (Supplementary Information).

Coordination polymers formed from metal ions and carboxylate-functionalized building blocks are well known in transition metal coordination chemistry[18–22]. They are typically prepared as macroscopic crystalline materials by one of several methods, including slow diffusion of solvent into solutions consisting of precursors,
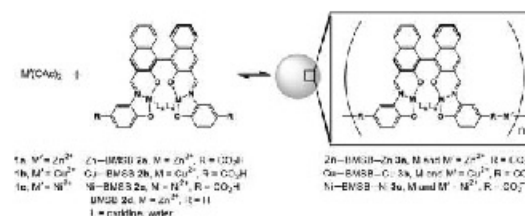

Figure 1 | Preparation of particles 3a–c. Addition of diethyl ether or pentane into the reaction mixture containing 1 and 2 in pyridine results in particle formation and precipitation. Addition of excess pyridine dissolves the particles and redisperses the ligand and metal ion building blocks. The reaction is not truly reversible as written because the M' ions can coordinate pyridine. BMSB, binapthyl bis-metallo-tridentate Schiff base.

[1]Department of Chemistry and Institute for Nanotechnology, Northwestern University, 2145 Sheridan Road, Evanston, Illinois 60208-3113, USA.
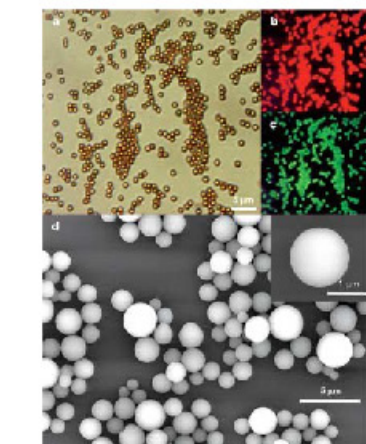
Figure 2 | Images of the spherical microparticles Zn–BMSB–Zn (3a). These have an average diameter of $1.60 \pm 0.47\ \mu m$ (s.d., $n = 100$) as determined by SEM and $1.72\ \mu m$ as determined by DLS. Images were obtained by optical microscopy (**a**), fluorescence microscopy (**b**, **c**) and SEM (**d**; inset in **d** is a high-resolution, zoom-in image).

Figure 3 | SEM and optical microscopy images of example micro- and nanoparticles formed through the infinite coordination polymer strategy, and the proposed cluster-fusion growth mechanism. a–c, SEM images monitoring the growth process for Zn–BMSB–Zn (3a). **a**, Image of an early intermediate cluster formed by aggregation of small particles. The small particles become oblong as they merge with each other. **b**, Image of an intermediate at a later stage, showing surface annealing. **c**, Image of a fully formed spherical particle. **d**, Dark-field optical microscopy image of cluster aggregates (bottom) and a fully formed particle (top). **e**, A schematic representation of the proposed cluster-fusion growth mechanism. **f**, Image of spherical particles 3a with an average diameter of $190 \pm 60\ nm$ (s.d., $n = 50$) as determined by SEM and $176\ nm$ as determined by DLS. **g**, Image of spherical particles 3a with an average diameter of $780 \pm 230\ nm$ (s.d., $n = 50$) as determined by SEM and $575\ nm$ as determined by DLS.

Figure 4 | Optical properties of 3a. a, A photograph of a series of spherical particles Zn–BMSB–Zn 3a where the ancillary ligands have been systematically changed (left to right: L = dimethyl sulphoxide (DMSO), pyridine, N,N-dimethylformamide (DMF), acetone, methanol and water). All particles are dispersed in toluene except where L is water, in which case pure water was used. **b**, Emission spectra of this series of particles 3a. Excitation wavelength, 420 nm.

solvothermal synthesis, layering, and slow evaporation[18–22]. In our system, spherical microparticles Zn–BMSB–Zn, **3a** (Fig. 2), instead of the more typically observed macroscopic materials, form within one hour upon slow diffusion of diethyl ether into a precursor solution containing homochiral Zn–BMSB (**2a**) and Zn(OAc)₂ (**1a**) in a 1:1 ratio in pyridine at room temperature. The addition of diethyl ether or pentane to the polar precursor solution results in precipitation due to the low solubility of the particles in non-polar media. The resulting particles are stable in organic solvents (toluene, methanol, DMF and dimethyl sulphoxide (DMSO)), in water and in the dried state.

Optical microscopy (Fig. 2a), fluorescence microscopy (Fig. 2b and c), and scanning electron microscopy (SEM, Fig. 2d) images of example compositions show spherical particles with an average diameter of $1.60 \pm 0.47\ \mu m$. Average particle size was also measured by dynamic light scattering (DLS) and was in agreement with the SEM determined value. The chemical composition of the particles was determined by energy dispersive X-ray spectroscopy and elemental analysis. Control experiments with **2d**, which has no carboxylate groups, show that the coordination polymer and, therefore, microparticles, will not form in the absence of the carboxylate groups. Infrared spectra taken before and after formation of the particles show that the carboxylate groups are coordinating to metal ions, as evidenced by a shift in CO stretching frequency from 1,653–1,659 cm⁻¹ for the monomeric unbound forms (**2a–c**) to 1,597–1,605 cm⁻¹ for the polymer particles (**3a–c**). In addition to the aforementioned control experiments and Fourier-transform infrared spectroscopy, we also find that ¹H and ¹³C NMR spectroscopy, and electrospray ionization mass spectrometry, are all consistent with the proposed mode of polymerization (see Supplementary Information). Featureless powder X-ray diffraction data for these particles show that they are amorphous and not crystalline materials. The
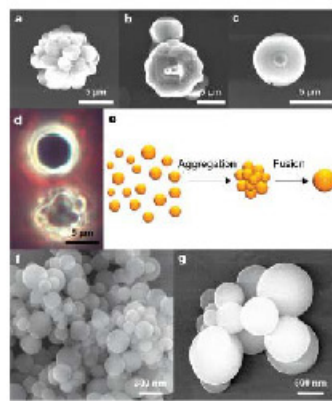
Zn–BMSB–Zn particles (**3a**) are fluorescent in the red and green regions of the spectrum (Fig. 2b and c) as a result of the highly fluorescent BMSB building block, **2a** (ref. 24). Indeed, the emission spectra of the polymer particles **3a** and monomer building block **2a** are nearly identical (Supplementary Fig. 2).

When pentane is used as an initiation solvent instead of diethyl ether, larger spherical microparticles ($\sim 5\ \mu m$) form (Fig. 3a–d, Supplementary Fig. 4). Under these synthesis conditions, the growth of the particles can be observed by taking aliquots from the synthesis mixture at various stages and characterizing the particles by SEM and optical microscopy. The observations reveal two kinds of intermediate particles: clusters formed by aggregation of small particles, and a fused version of such clusters. At early stages of the reaction, the clusters of smaller particles are readily observable (Fig. 3a and 3d, bottom); the clusters then slowly anneal into single particles with smoother surfaces (Fig. 3b) and ultimately form uniform spherical particles (Fig. 3c and 3d,top). These observations suggest a two-step cluster-fusion growth mechanism (Fig. 3e), where several small particles first aggregate to form large cluster particles, which in a second step undergo intra-particle fusion to yield large uniform spherical particles. This can occur because of the reversible nature of the metal coordination chemistry, allowing the system to anneal into a smooth particle. The cluster fusion step can involve dozens of particles or only a few, depending upon conditions, and the ultimate size of the large spherical particles depends upon the number of smaller particles involved in the fusion process. Although they cannot be completely ruled out, physical effects probably play a
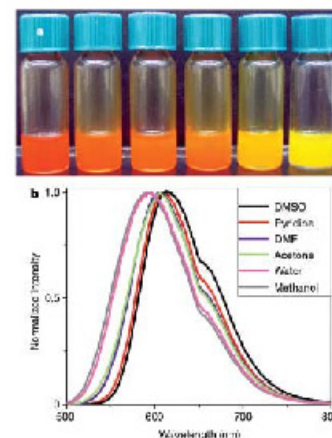
more minor role in the polymerization process as the reaction mixture is not stirred while the particles are forming.

The rate of addition and type of initiation solvent allow control of particle size. Fast addition results in nanoscale particles by quenching the growth process at an early stage in the reaction. Nanoparticles of **3a** with an average diameter of $190 \pm 60\ nm$ (Fig. 3f) could be prepared by the rapid addition of diethyl ether to the reaction mixture of **2a** and **1a** in pyridine. In contrast, the fast addition of pentane as the initiation solvent under nearly identical conditions resulted in particles with an average diameter of $780 \pm 230\ nm$ (Fig. 3g). The polarity of the solvent affects the solubility of the resulting particles and, therefore, their average size. This size control will probably be refined as this process evolves.

We also investigated the utility of this method for producing spherical particles of coordination polymers with other metal ions such as Cu²⁺ and Ni²⁺ (see Supplementary Information). Spherical nanoparticles of Cu–BMSB–Cu (**3b**), synthesized from the fast addition of pentane to a precursor solution containing Cu–BMSB (**2b**) and Cu(OAc)₂·(H₂O) (**1b**) in pyridine, have diameters similar to Zn–BMSB–Zn particles (**3a**) prepared via an analogous procedure. Slow diffusion of pentane into a precursor solution containing **2b** and **1b** yields particles that are on average significantly larger than the particles formed from the fast addition method. Similarly, the reaction between Ni–BMSB (**2c**) and Ni(OAc)₂·4(H₂O) (**1c**) gives spherical particles Ni–BMSB–Ni (**3c**). In contrast to **3a**, particle compositions **3b** and **3c** are not fluorescent because they are not made of fluorescent BMSB building blocks.

The ancillary ligands (L in Fig. 1) in these polymer particles allow the particles' physical properties to be controlled by adjusting the electronic nature of the metals to which they are coordinated. For example, a red toluene suspension of the spherical particle

composition of **3a** turns yellow when methanol is added to the reaction vessel. This colour change is attributed to the replacement of the pyridine ligand on the Zn metal centres with methanol. If the solvent is removed from this complex and the particles are redispersed in toluene with DMSO (10% by volume), the yellow solution turns red owing to the formation of Zn–DMSO adducts. It is well known that isoelectronic monomers of this class of compounds exhibit characteristic red-shifts in the solution state as a function of the increasing σ-donor properties of the ancillary ligands[25]. The optical properties of the nanoparticles are highly dependent upon the type of coordinating ligands, and the effects of different ligands (DMSO, pyridine, DMF, acetone, methanol and water) can be observed with the naked eye (Fig. 4a). All reactions, with the exception of pyridine, which dissolves the particles (see above), appear to be completely reversible, and can be effected within seconds of introduction to the appropriate small molecule. Emission and diffuse reflectance spectra of this series of particle compositions demonstrate the reversibility of these reactions and the ability to fine-tune the optical properties of the particles through choice of ancillary ligands (Fig. 4b).

As BMSB building blocks can be prepared in enantiopure form and are important compounds in homogeneous catalysis[26], this new class of material may find use in asymmetric catalysis and chiral separations. In these applications, the small size of the particles results in a high overall surface area that ensures major advantages over bulk materials.

1. Bell, A. T. The impact of nanoscience on heterogeneous catalysis. Science 299, 1688–1691 (2003).
2. Wang, J., Gudiksen, M. S., Duan, X., Cui, Y. & Lieber, C. M. Highly polarized photoluminescence and photodetection from single indium phosphide nanowires. Science 293, 1455–1457 (2001).
3. Blanco, A. et al. Large-scale synthesis of a silicon photonic crystal with a complete three-dimensional bandgap near 1.5 micrometres. Nature 405, 437–440 (2000).
4. Cao, Y. C., Jin, R. & Mirkin, C. A. Nanoparticles with Raman spectroscopic fingerprints for DNA and RNA detection. Science 297, 1536–1540 (2002).
5. Bruchez, M. Jr, Moronne, M., Gin, P., Weiss, S. & Alivisatos, A. P. Semiconductor nanocrystals as fluorescent biological labels. Science 281, 2013–2016 (1998).
6. Taton, T. A., Mirkin, C. A. & Letsinger, R. L. Scanometric DNA array detection with nanoparticle probes. Science 289, 1757–1760 (2000).
7. Mirkin, C. A., Letsinger, R. L., Mucic, R. C. & Storhoff, J. J. A DNA-based method for rationally assembling nanoparticles into macroscopic materials. Nature 382, 607–609 (1996).
8. Elghanian, R., Storhoff, J. J., Mucic, R. C., Letsinger, R. L. & Mirkin, C. A. Selective colorimetric detection of polynucleotides based on the distance-dependent optical properties of gold nanoparticles. Science 277, 1078–1081 (1997).
9. Sun, S., Murray, C. B., Weller, D., Folks, L. & Moser, A. Monodisperse FePt nanoparticles and ferromagnetic FePt nanocrystal superlattices. Science 287, 1989–1992 (2000).
10. Horn, D. & Rieger, J. Organic nanoparticles in the aqueous phase—theory, experiment, and use. Angew. Chem. Int. Edn Engl. 40, 4331–4361 (2001).
11. Roscoe, S. B., Fréchet, J. M. J., Walzer, J. F. & Dias, A. J. Polyolefin spheres from metallocenes supported on noninteracting polystyrene. Science 280, 270–273 (1998).
12. Fu, H.-B. & Yao, J.-N. Size effects on the optical properties of organic nanoparticles. J. Am. Chem. Soc. 123, 1434–1439 (2001).
13. Henglein, A. Reduction of Ag(CN)₂⁻ on silver and platinum colloidal nanoparticles. Langmuir 17, 2329–2333 (2001).
14. Peng, X. et al. Shape control of CdSe nanocrystals. Nature 404, 59–61 (2000).
15. Chen, J., Herricks, T. & Xia, Y. Polyol synthesis of platinum nanostructures: control of morphology through the manipulation of reduction kinetics. Angew. Chem. Int. Edn Engl. 44, 2589–2592 (2005).
16. Jin, R. et al. Photoinduced conversion of silver nanospheres to nanoprisms. Science 294, 1901–1903 (2001).
17. Jin, R. et al. Controlling anisotropic nanoparticle growth through plasmon excitation. Nature 425, 487–490 (2003).
18. Seo, J. S. et al. A homochiral metal–organic porous material for enantioselective separation and catalysis. Nature 404, 982–986 (2000).
19. Rosi, N. L. et al. Hydrogen storage in microporous metal–organic frameworks. Science 300, 1127–1129 (2003).

20. Yaghi, O. M. et al. Reticular synthesis and the design of new materials. Nature 423, 705–714 (2003).
21. Evans, O. R. & Lin, W. Crystal engineering of NLO materials based on metal-organic coordination networks. Acc. Chem. Res. 35, 511–522 (2002).
22. Kosal, M. E., Chou, J.-H., Wilson, S. R. & Suslick, K. S. A functional zeolite analogue assembled from metalloporphyrins. Nature Mater. 1, 118–121 (2002).
23. Tabellion, F. M., Seidel, S. R., Arif, A. M. & Stang, P. J. Template and guest effects on the self-assembly of a neutral and homochiral helix. Angew. Chem. Int. Edn Engl. 40, 1529–1532 (2001).
24. Splan, K. E. et al. Photophysical and energy-transfer properties of (salen)zinc complexes and supramolecular assemblies. Eur. J. Inorg. Chem. 2348–2351 (2003).
25. Kilsä, K. et al. Anchoring group and auxiliary ligand effects on the binding of ruthenium complexes to nanocrystalline TiO₂ photoelectrodes. J. Phys. Chem B 108, 15640–15651 (2004).
26. Ruck, R. T. & Jacobsen, E. N. Asymmetric catalysis of hetero-ene reactions with tridentate Schiff base chromium(III) complexes. J. Am. Chem. Soc. 124, 2882–2883 (2002).

LETTERS

Slowing of the Atlantic meridional overturning circulation at 25° N

Harry L. Bryden[1], Hannah R. Longworth[1] & Stuart A. Cunningham[1]

The Atlantic meridional overturning circulation carries warm upper waters into far-northern latitudes and returns cold deep waters southward across the Equator[1]. Its heat transport makes a substantial contribution to the moderate climate of maritime and continental Europe, and any slowdown in the overturning circulation would have profound implications for climate change. A transatlantic section along latitude 25° N has been used as a baseline for estimating the overturning circulation and associated heat transport[2–4]. Here we analyse a new 25° N transatlantic section and compare it with four previous sections taken over the past five decades. The comparison suggests that the Atlantic meridional overturning circulation has slowed by about 30 per cent between 1957 and 2004. Whereas the northward transport in the Gulf Stream across 25° N has remained nearly constant, the slowing is evident both in a 50 per cent larger southward-moving mid-ocean recirculation of thermocline waters, and also in a 50 per cent decrease in the southward transport of lower North Atlantic Deep Water between 3,000 and 5,000 m in depth. In 2004, more of the northward Gulf Stream flow was recirculating back southward in the thermocline within the subtropical gyre, and less was returning southward at depth.

Some climate models suggest that the anthropogenic increase in atmospheric carbon dioxide will result in a slowdown of the Atlantic overturning circulation[5]. Coupled climate model runs that had the Atlantic overturning circulation shut off exhibited a cooling over northwest Europe with temperatures 4 °C lower than at present[6]. Thus, any indication of a slowdown in the Atlantic overturning circulation has profound implications for climate change. In March 2004 we deployed an array of moored instruments along 25° N to begin to monitor the overturning circulation[7] and in April–May we took a transatlantic hydrographic section along 25° N to provide an initial calibration for the time-series array measurements[8].

The 25° N transatlantic hydrographic section was occupied in 1957 (ref. 9), in 1981 (ref. 3) and again in 1992 (ref. 10). Analysis of these three occupations suggested that the overturning circulation and heat transport at 25° N had been reasonably constant with only relatively small changes in thermocline, intermediate and deep water transports[3,4]. In 1998, the 25° N section was again occupied[11], so the

section of 2004 marked the fifth complete transatlantic section along 25° N. Here we analyse the new 2004 section and the 1998 section using methods similar to those previously developed for the 1957, 1981 and 1992 sections[3,4] and examine the structure of the overturning circulation for all five sections.

Each section extends from the African continental shelf to the Bahama Islands (Fig. 1). The 1957 and 1992 sections were effectively along 24.5° N over the entire width of the Atlantic. The 1981, 1998 and 2004 sections angled southwestward from the African continental shelf at about 28° N to join the standard 24.5° N section at about 23.5° W. To take advantage of the continuous electromagnetic cable monitoring of Gulf Stream transport through the Florida Straits[12], the 1998 and 2004 sections angled northwestward at about 73° W to complete the section along 26.5° N.

The analysis calculates geostrophic velocities for each station pair along the section. A reference level of 3,200 dbar is used for station pairs east of the western boundary region where current meter observations suggest 1,000 dbar to be more suitable[4,13]. The transition between the two reference levels is identified from the distribution of dissolved oxygen concentration that marks the eastern edge of the boundary region[4] and ranges from 68.3° W to 70.6° W. The concept behind the analysis is to estimate the annual average overturning, so the annual averaged wind-driven surface Ekman transport and the annual averaged Gulf Stream transport through Florida Straits must be balanced by the overall southward geostrophic transport across the mid-ocean section. Thus a uniform reference level velocity is added everywhere along the section to force the mid-ocean geostrophic transport to balance the Gulf Stream plus Ekman transport. This approach assumes that the large-scale baroclinic interior flow does not vary on seasonal or shorter timescales; theoretical arguments and modelling results support such an assumption[3,4,5].

Gulf Stream transport through the Florida Straits has been reasonably constant at 32.2 Sv (1 Sv = 10^6 m³ s⁻¹) since 1980 (refs 12, 16) with a standard deviation in annual mean transport of 1.1 Sv. Sporadic estimates of Gulf Stream transport back to the 1960s[15–19] and cable estimates of transport since 2000 (ref. 20) show no evidence of changes in annual averaged transport through
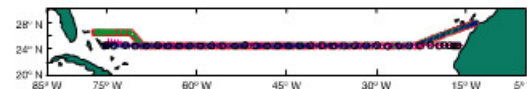

Figure 1 | Station positions for transatlantic hydrographic sections taken in 1957, 1981, 1992, 1998 and 2004. The 1957 and 1992 sections each went zonally along 24.5° N from the African coast to the Bahama Islands. Because of diplomatic clearance issues, the 1981, 1998 and 2004 sections angled southwestward from the African coast at about 28° N to join the 24.5° N section at about 23° W. The 1998 and 2004 sections angled northwestward at about 73° W to finish the section along 26.5° N.

[1]National Oceanography Centre, Empress Dock, Southampton SO14 3ZH, UK.